

## Aquarius Geophysical Model Function and Combined Active Passive Algorithm for Ocean Surface Salinity and Wind Retrieval

Simon Yueh, Wenqing Tang, Alexander Fore, Akiko Hayashi, Yuhe T. Song, and Gary Lagerloef

Jet Propulsion Laboratory, California Institute of Technology, Pasadena, California, USA

*Abstract*—This paper describes the updated Combined Active-Passive (CAP) retrieval algorithm for simultaneous retrieval of surface salinity and wind from Aquarius’ brightness temperature and radar backscatter. Unlike the algorithm developed by Remote Sensing Systems (RSS), implemented in the Aquarius Data Processing System (ADPS) to produce Aquarius standard products, the Jet Propulsion Laboratory’s CAP algorithm does not require monthly climatology SSS maps for the salinity retrieval. Furthermore the ADPS-RSS algorithm fully uses the National Center for Environmental Predictions (NCEP) wind for data correction, while the CAP algorithm uses the NCEP wind only as a constraint. The major updates to the CAP algorithm include the galactic reflection correction, Faraday rotation, Antenna Pattern Correction, and geophysical model functions of wind or wave impacts. Recognizing the limitation of geometric optics scattering, we improve the modeling of the reflection of galactic radiation; the results are better salinity accuracy and significantly reduced ascending-descending bias. We assess the accuracy of CAP’s salinity by comparison with ARGO monthly gridded salinity products provided by the Asia-Pacific Data-Research Center (APDRC) and Japan Agency For Marine-Earth Science And Technology (JAMSTEC). The RMS differences between Aquarius CAP and APDRC’s or JAMSTEC’s ARGO salinities are less than 0.2 psu for most parts of the ocean, except for the regions in the Inter-tropical Convergence Zone, near the outflow of major rivers and at high latitudes.

Global measurements of sea surface salinity (SSS) are important for studying the ocean circulation and water cycle and consequently for improving the estimates of seasonal to interannual climate predictions. Two L-band microwave remote sensing satellites, the Soil Moisture and Ocean Salinity (SMOS) mission (Font et al., 2009; Boutin et al., 2012; Reul et al., 2012) and the Aquarius/SAC-D mission (Lagerloef et al., 2008) are currently operating to make global observations of SSS.

Aquarius is a combined passive/active L-band microwave instrument developed to map the salinity field at the surface of the ocean from space (Lagerloef et al., 2008), and has been operating since August 25, 2011. The primary science objective of this mission is to monitor the seasonal and interannual variation of the large-scale features of the SSS field in the open ocean with a spatial resolution of 150 km and a retrieval accuracy of 0.2 practical salinity unit (psu) globally on a monthly basis.

The measurement principle is based on the response of the L-band (1.413 GHz) sea surface brightness temperatures ( $T_B$ ) to SSS (Swift and McIntosh, 1983; Yueh et al., 2001). To achieve the required accuracy, the impact of sea surface roughness, galactic radiation and Faraday rotation, along with several additional factors, impacting the observed brightness temperature, must be corrected to better than a few tenths of a degree Kelvin. To this end, Aquarius' radiometer measures the first three Stokes parameters to enable Faraday rotation correction using the Aquarius data itself (Yueh, 2000), and the scatterometer (1.26 GHz) is included to help correct for the surface roughness effect.

We describe in this article the modifications to the Combined Active-Passive (CAP) algorithm for the retrieval of SSS and wind from Aquarius data (Yueh et al., 2012; Yueh et al., 2013). The data used for analysis and error evaluation are described in Section 2. Section 3 describes the model functions of sea surface scattering and emission. The retrieval algorithm is

described in Section 4. The performance of the CAP algorithm has been assessed by comparison with the in situ data from ARGO (Section 5). The summary is provided in Section 6.

## II. DATA

### A. Aquarius Data

The standard Aquarius L2 product is operationally processed by the Aquarius Data Processing System (ADPS) and distributed by the Physical Oceanography Distributed Active Archive Center (PODAAC). The Aquarius instrument has three antenna beams, operating at about 29-, 38- and 46-degree incidence angles (LeVine et al., 2007). Each antenna beam has one radiometer (1.413 GHz), which measures the first three Stokes parameters of microwave radiation (Kraus, 1986). The three antenna feeds for radiometers are shared with the scatterometer (1.26 GHz), which acquires the normalized radar cross sections ( $\sigma_0$ ) for co- and cross-polarizations. The standard L2 product includes the Aquarius radiometer brightness temperatures and radar backscatter data as well as the SSS retrieved based on the algorithm developed by Remote Sensing Systems (RSS) (Meissner and Wentz, 2014).

### B. Argo Gridded Data

The Argo (Array for Real-time Geostrophic Oceanography) (Roemmich and the Argo Steering Team, 2009) project provides in situ salinity profiles over the global ocean through the deployment of over 3000 free-drifting profiling floats that measure salinity and temperature from near the surface to 2000 dbar. For the evaluation of CAP product, we use two monthly gridded ARGO data composed from float observations through optimal interpolation (OI), which are obtained from two sources. The first set is from the Asia-Pacific Data-Research Center (APDRC) of the International Pacific Research Center (IPRC) at the University of Hawaii (available from <http://apdrc.soest.hawaii.edu>). The second is available from Japan Agency for Marine-Earth Science and Technology (JAMSTEC) (available from <http://www.jamstec.go.jp/ARGO>) [Hosoda et al., 2010]. In contrast to the APDRC, which is solely composed of ARGO data,

JAMSTEC combines data from ARGO floats, Triangle Trans-Ocean Buoy Network (TRITON), and available conductivity-temperature-depth (CTD) casts.

The Argo OI products are monthly gridded products, and will be limited by the temporal and spatial sampling of Argo individual measurements. There is clear evidence that the Argo OI products are inaccurate in the Western Atlantic and Eastern Pacific freshwater pool possibly because of the lack of Argo samples or surface stratification (Tang et al., 2014).

### III. AQUARIUS GEOPHYSICAL MODEL FUNCTION

The ocean surface roughness will affect L-band microwave emissions ( $T_B$ ) and radar backscatter ( $\sigma_0$ ) and will also influence the reflection of galactic and atmospheric radiation. This section describes the geophysical model functions, relating  $T_B$  and  $\sigma_0$  to the wind speed, wind direction and significant wave height. The modeling of the reflected galactic and atmospheric radiation is described in Section IV.B. We have previously analyzed about 7 months of Aquarius data to develop the geophysical model functions (Yueh et al., 2013). Analyses were completed by performing the matchup of Aquarius data with the wind speed from the Special Sensor Microwave Imager/Sounder (SSMIS), wind direction from the National Center for Environmental Prediction (NCEP), Reynolds Sea Surface Temperature (SST) (Reynolds et al., 2007), and the Hybrid Coordinate Ocean Model (HYCOM) SSS (Cassignot et al., 2009). The matchup data were used to develop the geophysical model function (GMF) for radar  $\sigma_0$  and excess surface emissivity ( $\Delta e_p$ ):

$$\Delta e_p = \frac{T_{Bp} - T_{Bpflat}(T_s, SSS, \theta)}{T_s}, \quad (1)$$

where  $T_{Bflat}$  is the brightness temperature of flat-water surfaces computed using a weighted average of the water dielectric constant models by Klein and Swift (1977) and Meissner and Wentz (2004) for a given Reynolds SST ( $T_s$ ) and HYCOM SSS. The weighting coefficients are



chosen to reduce the salinity retrieval bias at low temperatures and are provided in Tang et al. (2013). The subscript “p” stands for polarization, vertical (V) or horizontal (H).

We have repeated the previous analysis (Yueh et al., 2013), but have included the data acquired up to June 2013. To minimize the effects of rain (Tang et al., 2013), we excluded any matchups with non-zero SSMI/S rain rate from our analysis. The rain-free matchups were grouped into bins with step size of 1 m in Significant Wave Height (SWH),  $1 \text{ ms}^{-1}$  in wind speed and 10 degrees in wind direction. The Aquarius data in each bin were averaged to represent the expected microwave response at the given SWH, wind speed and direction.

The Aquarius data binned as a function of the NCEP wind direction are illustrated in Figs. 1 and 2 for all antenna beams. Figure 1 plots the  $\sigma_0$  for VV, HH and VH polarizations in the top, middle, and bottom panels, respectively. We did not include the cross-polarized backscatter in (Yueh et al., 2013), because it is much noisier and requires much more data to reduce the uncertainty. With the addition of one more year of data, the binned VH data are still somewhat noisy, but has shown wind speed and direction dependence (bottom panels in Fig. 1).

There is interesting direction dependence in all polarizations: The upwind backscatter is larger than the crosswind backscatter for high winds ( $>10 \text{ ms}^{-1}$ ), but the relative amplitude changes at lower wind speeds ( $<8 \text{ ms}^{-1}$ ). The Negative Upwind-Crosswind (NUC) Asymmetry at low winds for VV and HH was reported in (Isoguchi and Shimada, 2009; Yueh et al., 2013), and now can also be found in the VH channel. The NUC feature is not expected to be a feature of Bragg scattering (Wu and Fung, 1972; Kudryavtsev et al., 2003) unless the directional spectrum of the ocean surface has the same NUC asymmetry. Its physical origin remains to be determined.

The major differences among the three polarization channels are the depth of directional modulation and wind speed dependence near the crosswind direction. The amplitude of Upwind-Crosswind (UC) difference is similar for all polarizations at less than  $10 \text{ ms}^{-1}$  wind speeds. However, the UC difference increases rapidly with wind speed for the co-polarizations (VV and

HH), while the UC difference for VH changes much less. At the wind speed of  $20 \text{ ms}^{-1}$ , the UC difference for VV and HH reaches about 4 to 5 decibels (dBs), and the UC difference for VH is a factor of two smaller than VV and HH, about 1 dB for beam 1 (29 degrees incidence angle) and 2 dB for beam 3 (46 degrees incidence angle).

The combined effect of a relatively larger UC asymmetry at all wind speeds and NUC asymmetry at low winds creates an interesting phenomenon for the VV polarization at the crosswind direction. This is particularly obvious for beam 3; it is found that at the crosswind direction (90 or 270 degrees) the beam-3 VV backscatter at a wind speed of  $5 \text{ ms}^{-1}$  is larger than that at 8, 10, 12 and  $15 \text{ ms}^{-1}$  wind speeds. In other words, the VV radar backscatter has negative wind speed dependence at the crosswind direction for VV over a certain range of wind speeds; the particular range depends on incidence angles or antenna beams (Fig. 1).

The excess surface emissivity also exhibits directional dependence (Fig. 2) with features essentially the same as those derived with much less data (Yueh et al., 2013). The emissivity for vertical polarization has positive UC asymmetry (upper panel) at wind speeds higher than  $12 \text{ m s}^{-1}$ , while that for horizontal polarization has negative asymmetry (middle panel.) For lower wind speeds ( $<10 \text{ ms}^{-1}$ ), it seems that the emissivity for vertical polarization also has NUC asymmetry, like the radar data.

The directional dependence of the excess surface emissivity is small for low winds and increases with wind speed. At a wind speed of  $20 \text{ ms}^{-1}$ , the peak-to-peak emissivity change is about 0.005, roughly corresponding to 1.5 K in brightness temperature. A major difference from the radar data is that there is no negative wind speed dependence at the crosswind direction because of a relatively smaller upwind-crosswind directional modulation.

The emissivity of the third Stokes parameter (Kraus, 1986) is illustrated in the bottom panels of Fig. 2. The data are much noisier than those for vertical and horizontal polarizations because of the errors in the ancillary data required to calibrate the third Stokes data (Yueh et al., 2013).

Nevertheless, the third Stokes clearly has sinusoidal direction dependence at wind speeds above  $15 \text{ ms}^{-1}$ , confirming the features derived using less data (Yueh et al., 2013).

In addition to the surface wind, we have found that the ocean waves also influence the  $\sigma_0$  and surface emissivity at L-band (Yueh et al., 2014). Their analysis included the National Oceanic and Atmospheric Administration (NOAA) WaveWatch-3 (WW3) Significant Wave Height (SWH) in the matchup data. The Aquarius data were binned as a function of the SWH at 1-m step as well as wind speed and direction. The directional dependence of the Aquarius data at each wind speed and SWH was analyzed, and it was concluded that the influence of the SWH on the wind direction dependence is small, about 10 percent of the directional amplitude.

Based on the analysis of the Aquarius data indicated above, we represent the Aquarius GMF by the following cosine series to model the impact of wind and waves on L-band  $\sigma_0$  and  $T_B$ :

$$\sigma_{0p}(w, \phi, SWH) = A_{0p}(w, SWH)[1 + A_{1p}(w)\cos\phi + A_{2p}\cos 2\phi] \quad (2)$$

$$\Delta e_p(w, \phi, SWH) = e_{p0}(w, SWH) + e_{p1}(w)\cos\phi + e_{p2}(w)\cos 2\phi \quad (3)$$

In the above equations, the subscript “p” indicates the polarization, which can be VV or HH for radar data and V or H for radiometer data. Note that we have neglected the impact of SWH on  $A_{1p}$ ,  $A_{2p}$ ,  $e_{p1}$  and  $e_{p2}$  because the number of samples in every wind direction bin for each wind speed and SWH are small for less frequent conditions (e.g., high winds and low SWH), making it difficult to derive these coefficients with consistent accuracy for all wind speed and SWH. When more Aquarius data become available, these coefficients will be more accurately modeled and considered for the next version of algorithm upgrade to incorporate the SWH impact on the directional dependence.

Given the GMF for excess surface emissivity, we use the following functional form for the radiometer model function, which relates the  $T_B$  to SSS, SST, SWH, wind speed and direction:

$$T_{Bp}(SSS, T_s, w, \phi, SWH, \theta) = T_{Bpflat}(SSS, T_s, \theta) + T_s \Delta e_p(w, \phi, SWH), \quad (4)$$

where  $\theta$  is the incidence angle.

We have derived the  $A_{1p}$ ,  $A_{2p}$ ,  $e_{p1}$  and  $e_{p2}$  coefficients from the data. Because their amplitudes are very close to those reported in (Figs. 4 and 5, Yueh et al., 2013), we therefore do not provide similar figures in this article. However more data have improved the estimation of these directional coefficients at above  $18 \text{ ms}^{-1}$  wind speeds. For radar data, we find that the  $A_1$  coefficient for HH polarization is about a factor of three larger than that for VV polarization, while the  $A_2$  coefficients of both polarizations are essentially the same. The negative values of  $A_2$  for wind speeds between 3 and  $8 \text{ ms}^{-1}$  signifies the NUC asymmetry discussed earlier. For radiometer data, the upwind-downwind asymmetry, represented by  $e_1$ , increases with increasing wind speed and turns out to be larger for vertical polarization than for horizontal. The amplitudes of  $e_{2v}$  and  $e_{2h}$  are about the same although the sign of  $e_{2h}$  is negative. The characteristics of  $e_{p1}$  and  $e_{p2}$  are similar to those of higher frequency (10-37 GHz) radiometer data (Yueh et al., 1999; Yueh et al., 2006; Yueh et al., 2008).

The cosine series fit of the data versus relative wind direction (e.g., Figs. 1 and 2) also produces the amplitude of  $A_{p0}$  and  $e_{p0}$  for each wind speed and SWH. The values of radar  $A_{p0}$  are illustrated in Fig. 3 versus the SSMI/S wind speed for 8 SWH ranges. The apparent influence of the SWH seems quite small for wind speeds lower than  $5 \text{ ms}^{-1}$  and increases with increasing wind speed. The characteristic of  $e_{p0}$  is very similar (Fig. 4). The tight correlation between the L-band  $A_{p0}$  and  $e_{p0}$  for low and moderate wind speeds ( $<7 \text{ ms}^{-1}$ ) indicates that they and the SSMIS wind speeds are all measure of surface roughness although at different length scales.

We find that it is more accurate and flexible to use tables together with interpolation or extrapolation for the computation of the model coefficients at any wind speed and SWH. The tables contain the values of the  $A_{p1}$ ,  $A_{p2}$ ,  $e_{p1}$  and  $e_{p2}$  at each  $1 \text{ ms}^{-1}$  from 0 to  $25 \text{ ms}^{-1}$  wind speeds, for each antenna beam and polarization. Linear interpolation and extrapolation of the table values are used to obtain the values of  $A_{pn}$  and  $e_{pn}$  at wind speeds below  $25 \text{ ms}^{-1}$ . For wind speeds above

25  $\text{ms}^{-1}$ , we applied additional exponential attenuation (Yueh et al., 2013) to reduce the directional modulation to zero for extreme high velocities as indicated in the high frequency radar and radiometer data. For  $A_{p0}$  and  $e_{p0}$ , they are tabulated as functions of wind speed and SWH at 1  $\text{ms}^{-1}$  and 1 m steps for each antenna beam and polarization. Bi-linear interpolation or extrapolation of the lookup table values is used to obtain the values of  $A_{p0}$  and  $e_{p0}$  at any wind speed and SWH.

#### IV. AQUARIUS CAP $T_A$ TO SALINITY PROCESSING

The processing flow for the Aquarius CAP retrieval is shown in Fig. 5. The scatterometer data will go through its calibration and retrieval processing (right branch in Fig. 5) to obtain an estimate of the surface wind speed (Yueh et al., 2012; Fore et al., 2013). The scatterometer wind retrieval algorithm using dual-polarization data, VV and HH, has been published in (Fore et al., 2013), and will not be repeated here.

In the following, we will describe the key steps for the radiometer data processing path, the left branch in Fig. 5, leading to the simultaneous retrieval of salinity, wind speed and direction. Section IV.A describes the processing of antenna brightness temperatures ( $T_A$ ) to surface brightness temperatures ( $T_B$ ). The required model for galaxy reflection correction as part of the  $T_A$  to  $T_B$  processing is presented in Section IV-B. The processing algorithm for salinity retrieval from surface TB and backscatter is described in Section IV.C.

##### A. Aquarius $T_A$ to $T_B$ Calibration

The Aquarius radiometers make partially polarimetric measurements to obtain the first three Stokes parameters, I, Q, and U (Kraus, 1986), which can be represented by a three-component vector,  $\bar{T}_A$ :

$$\bar{T}_A = \begin{bmatrix} I \\ Q \\ U \end{bmatrix} = \begin{bmatrix} T_V + T_H \\ T_V - T_H \\ U \end{bmatrix} \sim \begin{bmatrix} \langle |E_V|^2 \rangle + \langle |E_H|^2 \rangle \\ \langle |E_V|^2 \rangle - \langle |E_H|^2 \rangle \\ 2\text{Re}(E_V E_H^*) \end{bmatrix} \quad (5)$$

The first two Stokes parameters,  $I$  and  $Q$ , correspond to the sum and difference of the vertically polarized brightness temperature ( $T_V$ ) and horizontally polarized brightness temperature ( $T_H$ ).  $T_V$  and  $T_H$  are measures of the power of the vertically polarized electrical field ( $E_V$ ) and horizontally polarized electric field ( $E_H$ ), while the third Stokes parameter ( $U$ ) signifies the real part of the correlation between  $E_V$  and  $E_H$ . The angular brackets denote the ensemble average of the enclosed quantities.

The antenna temperatures ( $\bar{T}_A$ ), referenced at the antenna input, contain the contribution of the emission from sea surfaces, but also the emissions from atmosphere and many galactic radiation sources ( $T_{Aspace}$ ) as well as the effects of Faraday rotation by the ionosphere (Yueh et al., 2001). The following calibration equation allows the conversion of the antenna temperature to the brightness temperature on the top of ionosphere.

$$\bar{T}_{OI} = \bar{A}(\bar{T}_A - \bar{T}_{Aspace}) \quad (6)$$

$$\bar{T}_{Aspace} = \bar{T}_{Aglxd} + \bar{T}_{Asund} + \bar{T}_{Asunr} + \bar{T}_{Asuns} + \bar{T}_{Amoonr} \quad (7)$$

$T_{Aglxd}$  represents the direct emission from the galaxy into the antenna,  $T_{Asund}$  the direct emission of Sun into the antenna,  $T_{Asunr}$  the reflection of sun radiation by the sea surface near the specular direction,  $T_{Asuns}$  the diffused scattering of sun radiation by the sea surface, and  $T_{Amoonr}$  the reflection of moon radiation near the specular direction. The definition of each vector, signifying the contribution from each source, is the same as that described in Eq. (5). These quantities have been computed using ancillary information, including the galaxy radiation map, solar flux, and the positions of Sun and Moon. The contributions of these are relatively small in comparison with the surface roughness effects (winds and waves) for the Aquarius retrieval. Their values

have been included in the Aquarius L2 files based on the algorithm described in (Wentz and LeVine, 2012), and are deemed sufficiently accurate at this time. In the future when the effects of surface roughness have been significantly reduced, iterations to improve the modeling of space radiation terms might be necessary. The only term related to the sky radiation, not accounted for in Eq. (7), is the galactic radiation reflected by sea surfaces, which has been found to have a critical impact on the accuracy of the Aquarius Version 2 and SMOS retrievals (Reul et al., 2012), and will be treated with an improved algorithm described in the next section.

In Eq. (6), the  $\bar{\bar{A}}$  matrix accounts for the antenna pattern correction for the estimation of the brightness temperatures within the antenna footprint from the integrated surface radiation on Earth. The values of the  $\bar{\bar{A}}$  matrix used by the CAP processing are obtained by an optimization method to minimize the root mean square difference between the Aquarius data and the model brightness temperatures computed using the Total Electron Content (TEC) from the International Global Navigation Satellite System (GNSS) Service TEC data (2013) with a scaling factor to compute the TEC below the satellite (Yueh et al., 2013). The values of  $\bar{\bar{A}}$  matrix elements are listed in Table 1.

The correction algorithm for Faraday rotation effects uses the third Stokes data measured by the radiometer (Yueh, 2000). The first three Stokes parameters of the emission above the atmosphere and the ones from the top of ionosphere, denoted with the subscripts ‘OA’ and ‘OI’, respectively, are related to each other by (Yueh, 2000):

$$I_{OA} = I_{OI} \quad (8)$$

$$Q_{OA} = \sqrt{Q_{OI}^2 + U_{OI}^2 - U_{OA}^2} \quad (9)$$

Because the second Stokes parameter is much larger than the third Stokes parameter for ocean emission at Aquarius’ incidence angles,  $Q_{OA}$  can be estimated by neglecting  $U_{OA}$  with high accuracy:

$$Q_{OA} \approx \sqrt{Q_{OI}^2 + U_{OI}^2} \quad (10)$$

The worst-case error of the above approximation is about 0.01 K for Aquarius beam 1 with an incidence angle of about 29 degrees ( $Q \approx 20$  K) at high wind speeds near  $20 \text{ ms}^{-1}$  ( $U \approx 0.75$  K). Beams 2 and 3 operate at larger incidence angles with the value of  $Q$  reaching 30 to 40 K, and will have smaller approximation errors. This approximation for Faraday rotation correction eliminates the need to use ancillary wind products to estimate  $U_{OA}$ .

From  $I_{OA}$  and  $Q_{OA}$ , we obtain the brightness temperature on the top of atmosphere for vertical and horizontal polarizations by  $T_{OAV} = (I_{OA} + Q_{OA})/2$  and  $T_{OAH} = (I_{OA} - Q_{OA})/2$ . They are related to the surface brightness temperatures ( $T_{BP}$ ) by the radiative transfer equation

$$T_{OAP} = \tau [T_{BP} + r_p (T_d + T_{BC}) + T_{glxp}] + T_u \quad (11)$$

Here  $\tau$  is the atmospheric transmittance for the path along the line of sight from the surface to the satellite,  $T_d$  the atmospheric downwelling brightness temperature,  $T_u$  the atmospheric upwelling brightness temperature,  $T_{glxp}$  the reflected galactic radiation, and  $T_s$  the SST.  $T_{BC}$  is a constant and equals 3 K, representing the floor of the galactic emission. The reflectivity of the surface ( $R_p$ ) is related to the surface emissivity ( $e_p$ ) by

$$R_p = 1 - e_p = 1 - \frac{T_{BP}}{T_s} \quad (12)$$

From Eqs. (11) and (12), we can solve for  $T_{BP}$

$$T_{BP} = \frac{T_{OAP} / \tau - T_u / \tau - (T_d + \tau T_{BC} + T_{glxp})}{1 - \frac{T_d + \tau T_{BC}}{T_s}} \quad (13)$$

This equation includes the correction of atmospheric effects and reflected galactic reflection ( $T_{glxp}$ ). The values of  $T_d$ ,  $T_u$ , and  $\tau$  can be found in the Aquarius L2 files.



Note that the atmospheric radiation has much small angular variation than the galaxy radiation, which can change by several Kelvin from the galactic plane to the poles. Therefore the geometric optics approximation with the nominal small perturbation correction to change the effective reflectivity (Eq. 12) can provide an accurate correction for downwelling atmospheric radiation, while the reflection of galactic radiation requires a more accurate treatment.

#### *B. Reflection of Galactic Radiation*

The galaxy includes many bright radiation sources at L-band radiometer frequencies (1400-1427MHz) which has been allocated for radio astronomy observations (Kraus, 1986). The magnitude of these sources may reach several Kelvin for radiation from stars near the galactic plane. The dominant contribution of the galactic radiation is due to reflection by the sea surface into the main lobe of the Aquarius antenna pattern. The typical approach to model the reflection term is to use a Geometric Optics (GO) scattering model (Tsang et al., 1985), which accounts for the specular reflection by the surfaces with various orientation angles. It is also quite common to assume a Gaussian distribution for the sea surface slope. Although the GO scattering model with the Gaussian slope distribution is fairly accurate, residual model errors can be as large as a few tenths of Kelvin, resulting in substantial errors for the Aquarius salinity retrieval. A well-known negative consequence is the ascending and descending (A-D) bias observed in the Aquarius Version 2 (upper panels in Fig. 6) and SMOS products (Reul et al., 2012).

To account for the diffuse scattering by sea surfaces (Wu and Fung, 1972; Kudryavtsev et al., 2003) and the non-Gaussian distribution of ocean wave slopes, we have to address the reflection of galactic radiation more rigorously. In general the reflected galactic radiation received by Aquarius can be modeled as:

$$T_{glp} = R_p \int K_p(\theta_x, \theta_y) T_{sky}(\theta_x, \theta_y) d\theta_x d\theta_y \quad (14)$$

The galactic radiation,  $T_{sky}$ , weighted by the kernel  $K_p$ , is integrated over the angles,  $\theta_x$  and  $\theta_y$ , on the elevation and azimuth planes relative to the boresight of the antenna. The kernel  $K_p$

includes the effects of surface scattering and the Aquarius antenna pattern. The term outside of the integral,  $R_p$ , is the surface reflectivity at the Aquarius incidence angles.

We expand the kernel  $K_p$  by a series of Gaussian functions:

$$K_p = \sum_{n=0}^N a_n(w, SWH) g_n(\theta_x, \theta_y) \quad (15)$$

For the CAP Version 3 algorithm, we let the function  $g_n$  be isotropic Gaussian function. This allows us to account for the isotropic portion of diffused scattering effects, which typically have broader scatter patterns and lower peak amplitude than the GO scattering effects (Fig. 7). The anisotropic scattering effects will be investigated for the next version of the Aquarius retrieval algorithm. The half-power width of  $g_n$  is 5n degrees. Aquarius' antenna beamwidth is about 5 degrees, and therefore a step of 5 degrees for the width of  $g_n$  is adequate to model the combined smoothing effects of surface scattering and antenna pattern.

Substituting Eq. (15) into Eq. (14) results in

$$T_{glxp} = R_p \sum_{n=0}^N a_n T_{bgn} \quad (16)$$

where

$$T_{bgn} = \int g_n(\theta_x, \theta_y) T_{sky}(\theta_x, \theta_y) d\theta_x d\theta_y \quad (17)$$

In general, the expansion coefficient,  $a_n$ , is a function of wind speed, wave height, and other surface roughness parameters. The issue is that we don't know its functional expression. Rather than using typical two-scale scattering models for ocean surface scattering (Wu and Fung, 1972; Kudryavtsev et al., 2003), we use an empirical approach to estimate  $T_{glxp}$ .

From Eq. (16), we can recognize that  $T_{glxp}$  is a function of  $T_{bgn}$ , wind speed, SWH, surface reflectivity, and so on.

$$T_{glxp} = T_{glxp}(w, SWH, R_p, T_{bg0}, T_{bg1}, \dots, T_{bg6}) \quad (18)$$

We truncated the series expansion at  $N=6$  because the integration over  $\pm 30$  degrees around the boresight is sufficient to account for the diffused scattering effects.

The implication of Eq. (18) is that we can parameterize  $T_{glxp}$  by a list of variables, which can be computed or are available from ancillary data sources. The input variables,  $T_{bgn}$ , are related to Aquarius viewing geometry and galactic radiation map, and are not related to the surface roughness parameters,  $w$ , SWH, and  $R_p$ .

To obtain an approximate expression of  $T_{glxp}$  described by Eq. (18), we apply neural network techniques developed by several researchers to solve nonlinear inversion problems, such as the determination of particle-size in optical sensing (Ishimaru et al., 1990), inversion of snow parameters from passive microwave remote sensing (Tsang et al., 1991), retrieval of rough surface parameters including the Root-Mean-Square (RMS) height and the correlation length (Ishimaru et al., 1992), and ice thickness inversion (Kwok et al., 1995).

The Multi-layer Perceptron (MP) (Lippmann, 1987) for the neural network has worked well for these applications and we use it for the modeling of  $T_{glxp}$ . A three-layer perceptron network trained with the backpropagation algorithm is used in this investigation (Rumelhart, et al., 1986). It consists of two hidden layers and one output layer as shown in Fig. 8. The output layer has two output nodes,  $T_{glxV}$  and  $T_{glxH}$ , for V and H polarizations.

When an input vector is fed into the network, each input element is multiplied by a weight and summed to be used as the input vector of the next layer. This sum, which is called the “net” or the “activation”, will pass through the node, represented by a nonlinear transfer function. Here the sigmoidal function is used for the transfer function (Rumelhart et al., 1986). The output vector of the first hidden layer is then used as the input vector for the second hidden layer. The same process is repeated until the output nodes are reached. The optimization of the inter-connection weights is based on reduction of the difference between the actual output vector (the vector produced by the network) and the desired output vector (the vector which the actual

output vector wants to converge to) and is based on the backpropagation algorithm (Rumelhart et al., 1986).

The training dataset is developed using the following procedure. For each Aquarius data block in the L2 files, we compute the model surface brightness temperature ( $\tilde{T}_{BP}$ ) using the GMF described in Eq. (4) with the scatterometer wind speed ( $w$ ), NCEP wind direction, Reynolds SST, and HYCOM SSS as inputs. The model reflectivity  $\tilde{R}_p$  is then computed as  $1 - \tilde{T}_{BP}/T_s$ . These two model quantities along with the atmospheric emission and transmittance allow the estimation of the reflected galactic radiation by:

$$\tilde{T}_{glxP} = (T_{OAp} - T_u) / \tau - \tilde{R}_p (T_d + T_{BC}) - \tilde{T}_{BP} \quad (19)$$

Each training data record includes  $\tilde{T}_{glxV}$  and  $\tilde{T}_{glxH}$  as the target parameters along with the input vector composed of  $w$ ,  $SWH$ ,  $\tilde{R}_p$ ,  $\tau$  and  $T_{bgn}$  (Fig. 8). Note that although we have included the relative azimuth angle and incidence angle as part of the input vector in Fig. 8, their contributions are negligible because the other inputs are isotropic and the incidence angle is essentially constant. They are kept so that we can maintain the same network structure or algorithm codes when the angular dependence is considered in the future. The backpropagation algorithm requires a large set of training data. We decide to train the neural network using the data acquired in 2012. The data in 2011 and 2013 are not used so that they can be used for consistency check.

We have tested a few options for the neural network modeling of the reflected galactic radiation. All options have been applied to the CAP retrieval processing to test their effectiveness. One option obtains one neural network for each antenna beam trained with the entire year of data acquired in 2012. We find that the global average of the ascending-descending (A-D) bias has been reduced to 0.1 psu or smaller most of the times, except the months of September and October, when the global average of A-D bias of about 0.3 psu is unchanged. The other option develops one neural network model for each month. This option allows us to reduce

the global average of A-D bias to  $<0.1$  psu for all months. The monthly dependence of the network coefficients is probably related to the change of the orientation of galactic plane with respect to the Aquarius beam look direction over time. Because we have not yet accounted for the directional scattering effects, it is likely some time dependence has to be included to compensate for the seasonal change in the orientation of galactic plane. (This is a subject for future investigation). For both options, we have also used a thinned dataset, only one day of data from every five days of Aquarius data for training. The results from the thinned dataset are slightly noisier, but are essentially the same as that from the training with the full dataset in 2012. This indicates that the training of neural networks has converged.

For the CAP V3.0 processing, we decided to use the monthly neural network for retrieval processing because of the much smaller A-D bias for the months of September and October. The computed  $T_{glxp}$  from the neural network model is illustrated in Fig. 9. Note that only the data in 2012 were included in the training dataset. The computed values for the data in 2011 and 2013 are fairly similar, indicating the consistency of the neural network models. We don't anticipate large interannual differences because large annual variability of wind speed and SWH is not expected.

We have confirmed that the ascending-descending bias of a few tenths of psu have been reduced (Fig. 6) using the neural network model for  $T_{glxp}$  correction. There are still some systematic residuals (bottom panels of Fig. 6), but they are similar in both months and are probably not related to the reflection of galactic radiation. For example, the negative A-D bias in the North Atlantic to the west of Europe and the positive A-D bias in the East China Sea are likely the result of radio frequency interference. They will be the subject of future research and model improvement for roughness, rain, wave direction and so on.

### *C. SSS and Wind Retrieval*

The CAP algorithm retrieves the salinity and wind simultaneously by finding the best-fit solution to minimize the difference between the Aquarius data and the model functions described

in Eqs. (2)-(4). The earlier versions of the CAP algorithm (Yueh and Chaubell, 2012; Yueh et al., 2013) use different functional forms for the cost function. After gaining more knowledge about the characteristics of the Aquarius L-band microwave data, particularly the weak response of radar backscatter to wind speed near the crosswind direction, we included the last two additional terms in Eq. (20) to constrain the wind speed and direction solutions primarily for near the crosswind directions. The cost function for the CAP Version 3 algorithm is

$$C_{ap}(w, \phi, SSS) = \sum_{p=V,H} \frac{(T_{Bp} - T_{Bpm})^2}{\Delta T^2} + \sum_{p=VV,HH} \frac{(\sigma_{0p} - \sigma_{0pm})^2}{(\gamma_p \sigma_{0p})^2} + \frac{(w - w_{NCEP})^2}{\Delta w^2} + \frac{\sin^2((\phi - \phi_{NCEP})/2)}{\delta^2} \quad (20)$$

The weighting factors for the Aquarius data are set according to the expected measurement and modeling uncertainties. We let  $\Delta T$  be the Noise-Equivalent-Delta-T (NEDT) of radiometer and  $\gamma_p$  be 1.4 times of the radar measurement sensitivity ( $k_{pc}$ ). The values of NEDT and  $k_{pc}$ , a function of signal-to-noise ratio, have been pre-computed and saved in the Aquarius L2 data files. The value of  $\Delta w$  is  $1.5 \text{ ms}^{-1}$ , a rather weak constraint because the accuracy of CAP wind speeds is estimated to be about  $0.7 \text{ ms}^{-1}$  (Yueh et al., 2013). The value of  $\delta$  is 0.2, which will constrain the wind direction to be within an RMS deviation of 11 degrees from the NCEP wind direction. Our previous analysis (Yueh et al., 2013) indicates that the directional accuracy of the CAP algorithm is about 10 degrees or better for wind speeds of  $15 \text{ ms}^{-1}$  or above. The effect of the last term will not impact the accuracy of the CAP wind direction retrieval for high winds, but will help constrain the wind direction solution for low winds, for which the L-band data have a weak response to wind direction (Figs. 1 and 2).

We have applied a modified Levenberg-Marquardt algorithm (Burton et al., 1999) to find the local minima of the cost function. The details of the minimization process and method to remove ambiguous solutions are described in (Yueh et al., 2013) and will not be repeated here.

## V. ERROR ANALYSIS

We have assessed the accuracy of Aquarius CAP products by comparison with the SSMI/S wind speed and in situ salinity data from APDRC and JAMSTEC gridded products. Detailed comparison of the Aquarius SSS for each antenna beam and gridded products with the in situ data from tropical moorings, Argo floats and Argo gridded products and the influence of many data flags can be found in (Tang et al., 2014). The assessment was performed using the Aquarius V2.5.1 data. We expect the conclusion on the performance of CAP algorithm to be applicable to the Aquarius V3.0 data because the Aquarius V3.0 data has the same antenna  $T_A$  and radar  $\sigma_0$  as those in the Aquarius V2.5.1. The changes from Aquarius V2.5.1 to V3.0 data are small with updates to data flags in the Aquarius L2 data, but no changes to the  $T_B$  and  $\sigma_0$  calibration.

For the accuracy of wind retrieval, we computed the Root-Mean-Square (RMS) difference between the CAP and SSMI/S wind speeds, and find its value to be about  $1 \text{ ms}^{-1}$ . We also applied the triple collocation analysis using the SSMI/S, CAP and ECMWF winds (Stoffelen, 1998; Vogelzang et al., 2011). The results indicate that the accuracy of CAP wind speed is essentially the same as that of SSMI/S wind speed, about  $0.7 \text{ ms}^{-1}$ , and less than the  $0.9 \text{ ms}^{-1}$  error for the ECMWF. The result of the triple collocation analysis based on V2.5.1 data is the same as what was reported in (Yueh et al., 2013), and hence we don't include similar tables or figures in this paper. The result also justifies the choice of  $1.5 \text{ ms}^{-1}$  for the  $\Delta w$  weighting factor in Eq. (20).

The accuracy of wind speed retrieved from the Aquarius scatterometer dual-polarized (VV and HH) data is also excellent (Fore et al., 2013). The RMS accuracy of scatterometer wind speed is about  $0.9 \text{ m s}^{-1}$  estimated using the triple collocation analysis (Fore et al., 2013). Although the scatterometer backscatter has shown weak dependence on the direction below  $8 \text{ m s}^{-1}$ , this characteristic in fact becomes beneficial for wind speed retrieval. Because of its excellent accuracy, its use for galactic correction is feasible (Fig. 8). In addition, the L-band wind speed from Aquarius will also be a very good reference for the future calibration of data from the

NASA Soil Moisture Active-Passive (SMAP) and Cyclone Global Navigation Satellite System (CGNSS) Missions.

Detailed error analysis of the Aquarius salinity products has been performed by Tang et al. (2014). Their comparison with the in situ data from Argo floats and moorings has been reported for time series and monthly gridded products. They have also indicated biases and root-mean-square difference (RMSD) of the SSS from each Aquarius beam.

For this article, we will focus on the assessment of monthly gridded products by comparison with the APDRC and JAMSTEC monthly gridded salinity products. We generated the CAP monthly average gridded products on a 1 by 1 degree grid using the optimal interpolation method: The Aquarius data within 110 km search radius of every grid point are weighted by a Gaussian function with half-power at 75 km from the grid point.

We computed the bias between CAP and APDRC as the differences of monthly averages from the September 2011 to September 2013 (Fig. 10). The bias is mostly between plus and minus 0.2 psu, except for regions near the Inter-Tropical Convergence Zone (ITCZ) and outflows from major rivers, such as Amazon, Congo, and Ganga. The bias is either due to the impact of rain, surface stratification or salinity bias in the CAP or APDRC SSS products.

We compared the RMS amplitude of anomaly over the 2-year period (Fig. 11). The mean of monthly averages is computed, and the anomaly is the deviation of the monthly average from the 24-month mean. The RMS amplitude of anomaly is computed as the RMS average of the anomalies over 24 months. In the following discussions, we will denote  $S_{\text{ARGO}}$  and  $S_{\text{AQ}}$  as the APDRC and Aquarius CAP SSS anomalies, respectively. The spatial pattern of the RMS amplitude of Aquarius CAP SSS anomaly ( $S_{\text{AQ}}$ ), particularly around the ITCZ, is strikingly similar to that of the APDRC product ( $S_{\text{ARGO}}$ ). This suggests that Aquarius and APDRC have observed similar physical processes although with different amplitude. The visual correlation is



supported by the high correlation coefficient between  $S_{AQ}$  and  $S_{ARGO}$  illustrated in Fig. 12. The correlation coefficient could be 0.8 or higher in many regions.

We find over most parts of the global ocean away from the ITCZ and river outflows that the RMS amplitudes of  $S_{AQ}$  and  $S_{ARGO}$  are quite small in the range of 0.1 to 0.2 psu (Fig. 11). A small amplitude in the APDRC anomaly means that these regions are quite “stable” with small temporal salinity variability. Since the Aquarius CAP SSS also has small anomalies, we can conclude that the Aquarius CAP retrieval over time is consistent with the APDRC to about 0.1 to 0.2 psu over 2 years. Furthermore, some of the regions with small anomalies also have strong correlation (Fig. 12), suggesting that the small anomaly in the Aquarius retrieval for these regions is physical signal of ocean processes, not noise. Based on the coherency between Aquarius and APDRC, it is likely that the accuracy of monthly-averaged CAP product has reached 0.2 psu or smaller at least for the regions of small anomalies (Fig. 11).

However Aquarius anomaly generally has larger amplitude, and reaches as large as 0.5 psu in the ITCZ (Fig. 11), while the APDRC could be a factor two smaller. Many of these regions in the Pacific, Indian Ocean and Atlantic also have high correlation (Fig. 12). If the larger amplitude in the Aquarius anomaly is due to noise (uncorrelated), then the correlation should be low (0.5 or smaller). For the regions with large anomaly and high correlation coefficient (larger than 0.8), the observations by Aquarius and APDRC are probably both accurate, and the differences can possibly be attributed to the surface stratification in the top few meters of oceans.

For high latitudes with cold waters, the Aquarius salinity is not expected to be as accurate because of a small sensitivity of  $T_B$  to salinity changes. The standard deviation of the differences,  $S_D(=S_{AQ}-S_{ARGO})$ , at high latitudes, particularly near the Antarctic, is about 0.3 psu or larger (Fig. 13). Because the correlation is low (Fig. 12) and the APDRC anomaly is small (Fig. 11), we can conclude that the relatively large difference in the regions south of 50 degrees south latitude is essentially caused by the noise or error in the Aquarius retrieval.

Because there is a correlation between the Aquarius and APDRC anomalies, their differences ( $S_D$ ) could be an overestimation of the error in the Aquarius CAP SSS. One method to estimate the standard deviation of uncorrelated differences is to combine the estimate of anomaly amplitude and correlation together. Because there is correlation between them, we can decompose  $S_{AQ}$  into correlated and uncorrelated components:

$$S_{AQ} = aS_{ARGO} + S_N \quad (21)$$

Here “a” is a scaling coefficient and  $S_N$  is a random uncorrelated component. The correlation (Fig. 12) between  $S_{ARGO}$  and  $S_{AQ}$  can be expressed as

$$\rho = \frac{a\sigma_{ARGO}^2}{\sqrt{\sigma_{ARGO}^2\sigma_{AQ}^2}} = \frac{a\sigma_{ARGO}}{\sigma_{AQ}} \quad (22)$$

where  $\sigma_{AQ}$  and  $\sigma_{ARGO}$  are the standard deviations of  $S_{AQ}$  and  $S_{ARGO}$ , respectively. From them, we can derive  $\sigma_N$ , the standard deviation of  $S_N$ ,

$$\sigma_N = \sigma_{AQ}\sqrt{1-\rho^2} \quad (23)$$

The magnitude of  $\sigma_N$  is about 0.1 psu on average and mostly smaller than 0.15 psu (Fig. 14), except near the regions of high precipitation or evaporation and major river outflows. Over a large portion of the ocean,  $\sigma_N$  is 0.05 psu or smaller. The excellent agreement (i.e., small  $\sigma_N$ ) with the APDRC strongly suggests that Aquarius has the capability to track the change of seasonal change of salinity to about 0.1 psu level in the tropics and mid-latitudes.

By comparison, the standard deviation of the differences between  $S_{AQ}$  and  $S_{ARGO}$  illustrated in Fig. 13 is

$$\sigma_D = \sqrt{(a-1)^2\sigma_{ARGO}^2 + \sigma_N^2} > \sigma_N \quad (24)$$

It is always larger than  $\sigma_N$ , and is mostly smaller than 0.2. The difference between what are illustrated in Figs. 13 and 14 is due to the difference of the correlated components.

The average bias between Aquarius and APDRC between 40 degrees N and 40 degrees S is indicated in Fig. 15. There is a small negative bias of about 0.05 psu in the Aquarius CAP SSS (CAP v2.5.1). The temporal variation of CAP retrieval bias seems to have a seasonal cycle with a peak-to-peak change of about 0.07 psu. The average bias in the ADPS data denoted by V2.5.1 produced using the RSS algorithm is larger and has a larger seasonal cycle ( $\sim 0.12$  psu). We performed similar comparison with JAMSTEC's ARGO, and the results are essentially the same (Fig. 16). Note that the CAP and ADPS algorithms use the HYCOM SSS to remove the global radiometer calibration bias on a daily basis. If the seasonal cycle in the retrieved bias is purely caused by the bias in the HYCOM, then both algorithms should have very similar bias. However, this is not the case. Therefore the differences between the CAP and ADPS retrieval biases are most likely due to differences in the algorithms, such as correction of the reflection of galactic radiation and geophysical model functions.

The RMS differences between Aquarius CAP and APDRC SSS have reached as low as about 0.18 psu in March 2012, and are smaller than or equal to 0.2 psu for 10 out of 24 months (lower panel in Fig. 15). The ADPS (V2.5.1) has a larger difference, always larger than 0.2 psu. Similar comparison has been made with the JAMSTEC SSS, and the conclusions are very similar (Fig. 16). However, the average bias with the JAMSTEC is slightly smaller, and the RMS differences are slightly larger.

The comparison with APDRC's and JAMSTEC's ARGO products suggests that the CAP algorithm outperforms the ADPS-RSS algorithm with better accuracy, and its performance is more consistent with a smaller variation seasonally; the RMSD of CAP varies between 0.18 to 0.24 psu, while the RMSD of the APDS-RSS algorithm varies between 0.21 and 0.3 psu.

## VI. SUMMARY

This paper describes the Version 3 of Aquarius' Combined Active-Passive (CAP) retrieval algorithm, which uses Aquarius' brightness temperature and radar backscatter for sea surfaces

for simultaneous retrieval of surface salinity and wind. The major updates to the CAP-V3 algorithm include the galactic reflection correction, Faraday rotation and Antenna Pattern Correction as well as the geophysical model functions (GMF) of wind and wave impacts. We use a series of expansion with Gaussian basis functions to approximate the scattering coefficients of ocean surfaces; this results in more accurate modeling of the reflection of galactic radiation and consequently reduces the ascending-descending bias significantly in the salinity retrievals. This improvement along with the Faraday Rotation and APC corrections leads to greatly reduced errors in the Aquarius CAP salinity retrievals.

We have assessed the accuracy of Aquarius CAP wind by performing comparison with the SSMI/S wind and triple collocation analysis. The root-mean-square difference with respect to the SSMI/S wind speed is about  $1 \text{ ms}^{-1}$ . The triple collocation analysis using the SSMI/S, CAP and ECMWF winds indicates that the accuracy of CAP wind speed is about  $0.7 \text{ m/s}$ , essentially the same as that of SSMI/S wind speed and less than the  $0.9 \text{ m/s}$  error for the ECMWF.

We have also assessed the accuracy of the Aquarius CAP salinity by comparison with the two ARGO monthly gridded salinity products obtained from the APDRC and JAMSTEC. The RMS differences between Aquarius CAP and APDRC or JAMSTEC gridded salinities are less than  $0.2 \text{ psu}$  for most parts of global oceans, except the regions in the Inter-tropical Convergence Zone (ITCZ), near the outflow of major rivers and at high latitudes. We find that the amplitude of monthly anomaly in the Aquarius CAP salinity is highly correlated with that in the ARGO data products in the ITCZ. The high correlation suggests that the difference between Aquarius CAP and ARGO salinities could be a result of surface stratification or other physical processes, resulting in differences between the salinity in the top few cm observed by Aquarius and a few meters below the surface measured by ARGO. Should this be the case, Aquarius and ARGO will provide complimentary information about the stratification in the ocean mixed layer. Accurate salinity measurements close to the surface is required to investigate the surface stratification process, and to validate the Aquarius salinity.

ACKNOWLEDGMENT

The work described in this paper was carried out by the Jet Propulsion Laboratory, California Institute of Technology under a contract with the National Aeronautics and Space Administration. The Aquarius data were obtained from the NASA Physical Oceanography Distributed Active Archive Center, <http://podaac.jpl.nasa.gov/aquarius>

REFERENCES

- Boutin, J., Martin, N., Yin, X.B., Font, J., Reul, N., Spurgeon, P., First Assessment of SMOS Data Over Open Ocean: Part II-Sea Surface Salinity, IEEE TRANSACTIONS ON GEOSCIENCE AND REMOTE SENSING, Volume: 50, Issue: 5, Pages: 1662-1675, DOI: 10.1109/TGRS.2012.2184546, May 2012.
- Burton, S. Garbow, Kenneth E. Hillstrom, Jorge J. More, 1999, Documentation for Minpack, Argonne National Laboratory, <http://www.netlib.org/minpack/>
- Chassignet, E.P., H.E. Hurlburt, E.J. Metzger, O.M. Smedstad, J. Cummings, G.R. Halliwell, R. Bleck, R. Baraille, A.J. Wallcraft, C. Lozano, H.L. Tolman, A. Srinivasan, S. Hankin, P. Cornillon, R. Weisberg, A. Barth, R. He, F. Werner, and J. Wilkin, 2009. U.S. GODAE: Global Ocean Prediction with the HYbrid Coordinate Ocean Model (HYCOM). Oceanography, 22(2), 64-75.
- Finlay, C. C., S. Maus, C. D. Beggan, T. N. Bondar, A. Chambodut, T. A. Chernova, A. Chulliat, V. P. Golovkov, B. Hamilton, M. Hamoudi, R. Holme, G. Hulot, W. Kuang, B. Langlais, V. Lesur, F. J. Lowes, H. Lühr, S. Macmillan, M. Manda, S. McLean, C. Manoj, M. Menvielle, I. Michaelis, N. Olsen, J. Rauberg, M. Rother, T. J. Sabaka, A. Tangborn, L. Tøffner-Clausen, E. Thébault, A. W. P. Thomson, I. Wardinski, Z. Wei and T. I. Zvereva, "International Geomagnetic Reference Field: the eleventh generation," *Geophys. J. Int.*, 183, pp. 1216–1230, 2010.

603 Font, J., A. Camps, A. Borges, M. Martin-Neira, J. Boutin, N. Reul, Y. H. Kerr, A. Hahne, and  
604 S. Mecklenburg. SMOS: The Challenging Sea Surface Salinity Measurement from Space,  
605 Proceedings of the IEEE, Vol. 98, No. 5, doi: 10.1109/jproc.2009.2033

606 Fore, A. G., S. H. Yueh, W. Tang, and A. K. Hayashi, Aquarius Wind Speed Products:  
607 Algorithms and Validation, IEEE Trans. Remote Sens., Vol. PP, No.99, pp.1,8, 0. doi:  
608 10.1109/TGRS.2013.2267616

609 Hosoda, S., T. Ohira, K. Sato, and T. Suga (2010), Improved description of global mixed-layer  
610 depth using Argo profiling floats, *J. Oceanogr.*, 66, 773-787.

611 Ishimaru, A., R. J. Marks II, L. Tsang, C. M. Lam, and D. C. Park, "Particle Size Distribution  
612 Determination Using Optical Sensing and Neural Networks," Opt. Lett., Vol. 15, No. 21,  
613 1221-1223, 1990.

614 Ishimaru, A., J. Hwang, K. Yoshitomi, and J. S. Chen, "Remote Sensing of Rough Surface  
615 Parameters Using Artificial Neural Network Technique," Proceedings of the International  
616 Geoscience and Remote Sensing Symposium, 1072-1073, Houston, Texas, May 1992.

617 Isoguchi, O. and M. Shimada, "An L-band Ocean Geophysical Model Function Derived from  
618 PALSAR," IEEE Trans. Geosci. Remote Sensing, Vol. 47, No. 7, pp. 1925-1936, July 2009.

619 Kraus, J. D., Radio Astronomy, 2nd. ed., 1986, Cygnus-Quasar Books, Powell, Ohio.

620 Kudryavtsev, V. N., D. Hauser, G. Caudal, and B. Chapron, "A semiempirical model of the  
621 normalized radar cross-section of the sea surface, 1. Background model," J. Geophys. Res.,  
622 Vol. 108, No. C3, 8054, doi: 10.1029/2001JC001003, 2003.

623 Kwok, R., S. V. Nghiem, S. H. Yueh, and D. D. Huynh, "Retrieval of thin ice thickness from  
624 multifrequency polarimetric SAR data," Remote Sens. of Environment, Vol. 51, No. 3, 361-  
625 374, 1995.

626 Lagerloef, G., F. R. Colomb, D. Le Vine, F. Wentz, S. Yueh, C. Ruf, J. Lilly, J. Gunn, Y. Chao,  
627 A. deCharon, G. Feldman, C. Swift, "The Aquarius/Sac-D Mission: Designed To Meet The

Salinity Remote-Sensing Challenge,” *Oceanography*, Vol. 21, no. 1, Special Issue: Sp. Iss. SI, pp. 68-81, Mar 2008.

LeVine, D.M., G.S.E. Lagerloef, R. Coloma, S. Yueh, and F. Pellerano, “Aquarius: An Instrument to Monitor Sea Surface Salinity from Space,” *IEEE Trans. Geosci. And Remote Sensing*, Vol. 45, No. 7, 2040-2050, July 2007.

Lippmann, R. P., “Introduction to Computing with Neural Nets,” *IEEE Trans. Acoust. Speech Signal Process*, 4-22, April 1987.

Klein, L., & Swift, C. (1977). An improved model for the dielectric constant of sea water at microwave frequencies. *IEEE Trans. on Antennas and Propagation*, 25, (1), 104 – 111.

Meissner, T. and F. Wentz, The Complex Dielectric Constant of Pure and Sea Water From Microwave Satellite Observations, *IEEE TGARS*, vol. 42 (9), 2004, 1836 – 1849.

Reynolds, R. W., T. M. Smith, C. Liu, D. B. Chelton, K. S. Casey, and M. G. Schlax, “Daily high-resolution blended analyses for sea surface temperature,” *J. Climate*, **20**, 5473-5496, 2007.

Reul, N, Tenerelli, J, Boutin, J, Chapron, B, Paul, F, Brion, E. Gaillard, F., Archer, O., Overview of the First SMOS Sea Surface Salinity Products. Part I: Quality Assessment for the Second Half of 2010, *IEEE TRANSACTIONS ON GEOSCIENCE AND REMOTE SENSING*, Vol. 50, No. 5, pp. 1636-1647, DOI: 10.1109/TGRS.2012.2188408, MAY 2012.

Roemmich, D., and the Argo Steering Team (2009), Argo: The challenge of continuing 10 years of progress, *Oceanography*, 22, 46–55.

Rumelhart, D. E., G. E. Hinton, and R. J. Williams, “Learning Internal Representations by Error Propagation,” *Parallel Distributed Processing (PDP): Exploration in the Microstructure of Cognition*, Vol. 1, Chapter 8, 318-362, MIT Press, Cambridge, Massachusetts, 1986.

Stoffelen A., “Toward the true near-surface wind speed: Error modeling and calibration using triple collocation,” *J. Geophysical Research*, Vol. 103, No. C4, pp. 7755-7766, April 15, 1998.

654 Swift, C. T. and R. E. McIntosh, "Considerations for Microwave Remote Sensing of Ocean  
655 Surface Salinity," IEEE Trans. Geosci. Remote Sensing," Vol. 21, No. 4, 480-491, 1983.

656 Tang, W., S. Yueh, A. Fore, G. Neumann, A. Hayashi, and G. Lagerloef, "The rain effect on  
657 Aquarius' L-band sea surface brightness temperature and radar backscatter," Remote Sensing  
658 of Environment, 137, pp. 147-157, 2013.

659 Tsang, L., J. A. Kong, R. T. Shin, Theory of Microwave Remote Sensing, John Wiley and Sons,  
660 1985.

661 Tsang, L., Z. Chen, S. Oh, R. J. Marks II, A.T.C. Chang, "Inversion of Snow Parameters for  
662 Passive Microwave Remote Sensing Measurements by a Neural Network Trained with a  
663 Multiple Scattering Model," Proceedings of International Geoscience and Remote Sensing  
664 Symposium, 1965-1966, Espoo, Finland, June 1991.

665 Vogelzang, J., Ad Stoffelen, Anton Verhoef, and Julia Figa-Saldaña, On the quality of high-  
666 resolution scatterometer winds, J. Geophysical Research, Vol. 116, C10033,  
667 doi:10.1029/2010JC006640, 2011.

668 Wentz, F. J. and D. M. LeVine, Version 2: Algorithm Theoretical Basis Document, Aquarius  
669 Salinity Retrieval Algorithm, RSS Technical Report 082912 August 29, 2012.

670 Wu, S. T., and A. K. Fung, "A noncoherent model for microwave emissions and backscattering  
671 from the sea surface," J. Geophys. Res., Vol. 77, No. 30, 5917-5929, 1972.

672 Yueh, S. H., R. West, W. J. Wilson, F. K. Li, E. G. Njoku, and Y. Rahmat-Samii, Error sources  
673 and feasibility for microwave remote sensing of ocean surface salinity, IEEE Trans. Geosci.  
674 Remote Sensing, 39, 1049-1060, 2001.

675 Yueh, S. H., W. J. Wilson, S. Dinardo, and F. K. Li, Polarimetric microwave brightness  
676 signatures of ocean wind directions, IEEE Trans. Geosci. Remote Sensing, Vol. 37, No. 2,  
677 pp. 949-959, 1999.



Yueh, S. H., W. Wilson, S. Dinardo, and S. V. Hsiao , “Polarimetric Microwave Wind Radiometer Model Function and Retrieval Testing for WindSat”, IEEE Trans. Geosci. And Remote Sensing, Vol. 44, No. 2, 584-596, March 2006.

Yueh, S. H., “Directional Signals in Windsat Observations of Hurricane Ocean Winds,” IEEE Trans. Geosci. Remote Sensing, Vol. 46, No. 1, 130-136, 2008.

Yueh, S. H., “Estimates Of Faraday Rotation With Passive Microwave Polarimetry For Microwave Remote Sensing Of Earth Surfaces,” IEEE Trans. Geosci. Remote Sensing, Vol. 38, No. 5, 2434-2438, September 2000.

Yueh, S. and J. Chaubell, “Sea Surface Salinity and Wind Retrieval using Combined Passive and Active L-Band Microwave Observations”, IEEE Trans. Geosci. Remote Sens., Vol. 50, No. 4, pp. 1022-1032, April 2012.

Yueh, S. H., W. Tang, A. Fore, G. Neumann, A. Hayashi, A. Freedman, J. Chaubell, and G. Lagerloef, L-band Passive and Active Microwave Geophysical Model Functions of Ocean Surface Winds and Applications to Aquarius Retrieval. *IEEE Trans. Geoscience and Remote Sensing*, 51 (9), 4619-4632, 2013, DOI: 10.1109/TGRS.2013.2266915.

Yueh, S., A. Fore, A. Freedman, M. J. Chaubell, W. Tang, and G. Neumann, Aquarius Scatterometer Algorithm Theoretical Basis Document, Version 1, March 15, 2012.

703

704

705 Table 1. Antenna pattern correction matrices for CAP V3.0 processing. (a) Beam 1, (b) Beam 2,  
 706 and (c) Beam 3. The tables include the values of matrix elements in the 3 by 3 matrices.

707

(a) Beam 1

1.045525	-0.038016	0.079827
-0.002615	1.080154	0.019636
-0.000837	-0.021868	1.085905

708

(b) Beam 2

1.050368	-0.033706	0.029473
0.000022	1.058856	-0.009407
-0.000915	0.013014	1.053165

709

(c) Beam 3

1.058510	-0.034170	0.028485
0.000577	1.049372	0.013427
-0.001530	-0.012219	1.029837

710

711

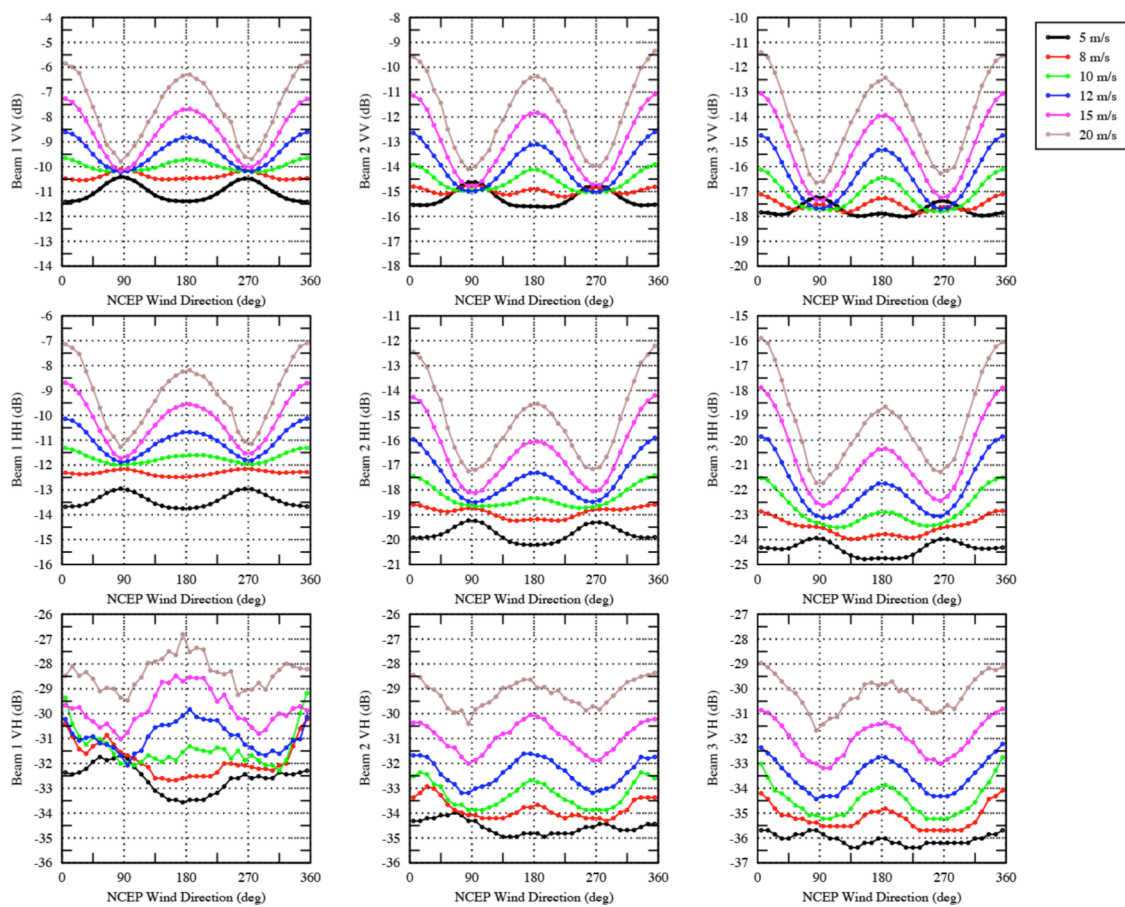


Figure 1. Aquarius radar backscatter versus the relative NCEP wind direction for 6 SSMIS wind speed bins. Data from three antenna beams are illustrated in three columns.

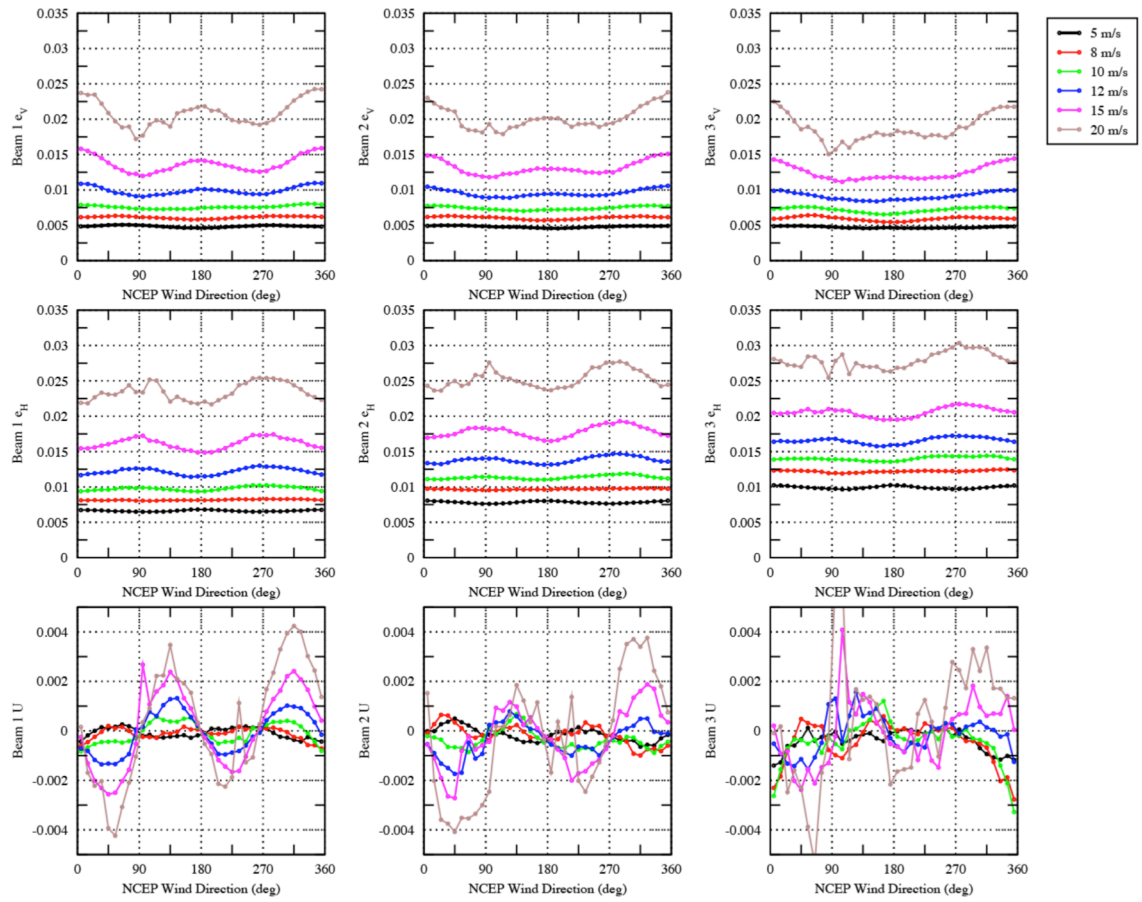


Figure 2. Aquarius excess surface emissivity versus the relative NCEP wind direction for 6 SSMIS wind speed bins. Data from three antenna beams are illustrated in three columns.

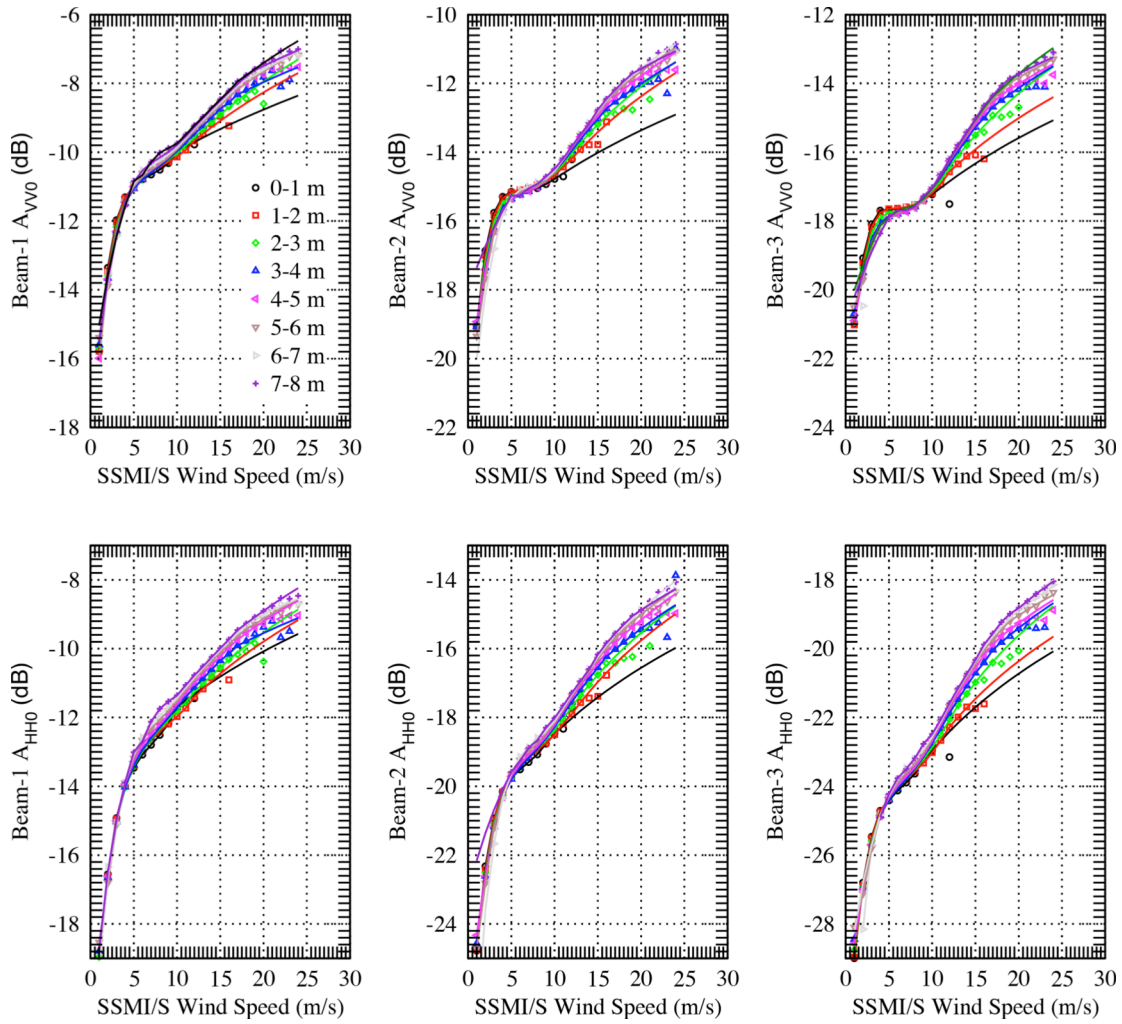


Figure 3. The Aquarius  $A_0$  coefficients versus the SSMI/S wind speed for 8 SWH bins. The smooth curves, connecting the dots, represent the interpolation or extrapolation of the binned  $A_0$  data computed at  $1\text{ ms}^{-1}$  steps.

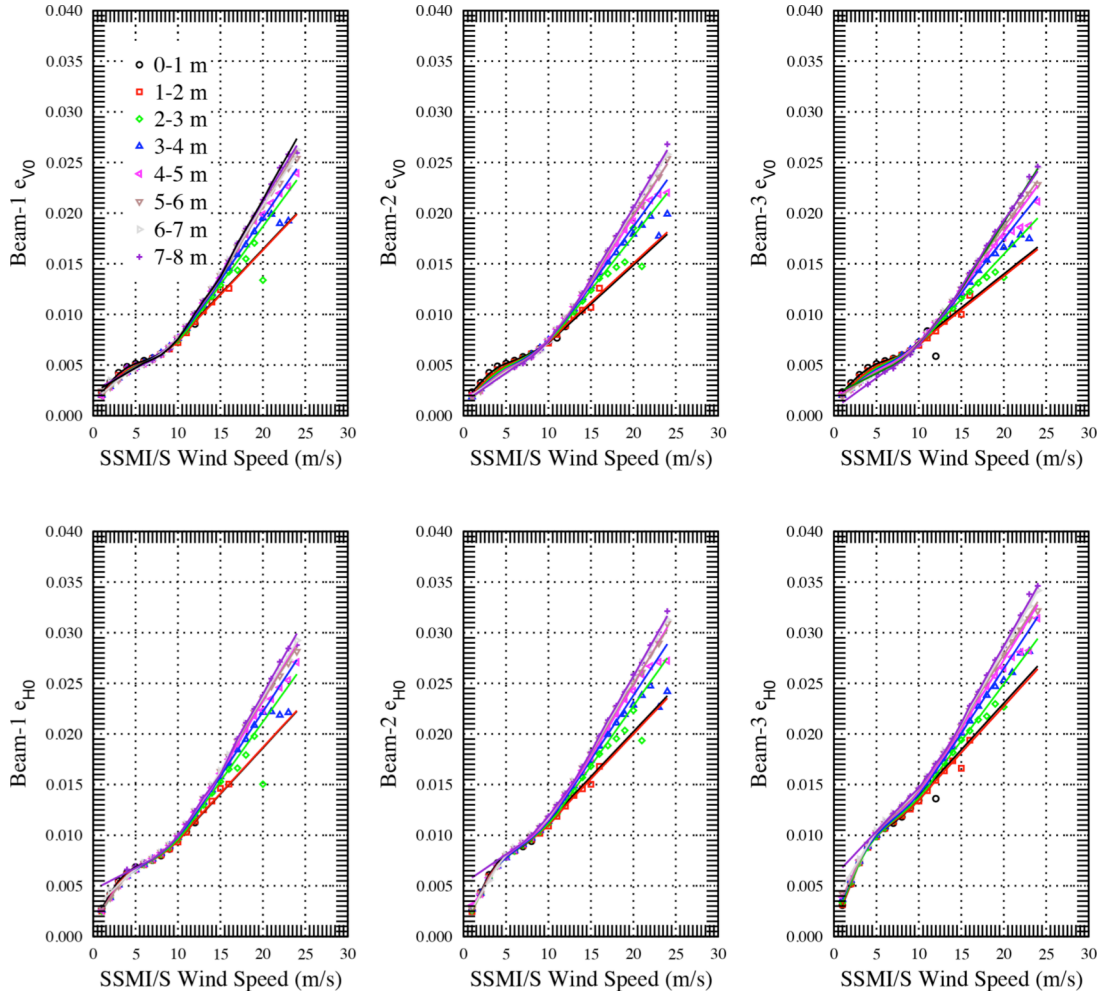


Figure 4. The Aquarius  $e_0$  coefficients versus the SSMI/S wind speed for 8 SWH bins. The smooth curves, connecting the dots, represent the interpolation or extrapolation of the binned  $e_0$  data computed at  $1\text{ ms}^{-1}$  steps.

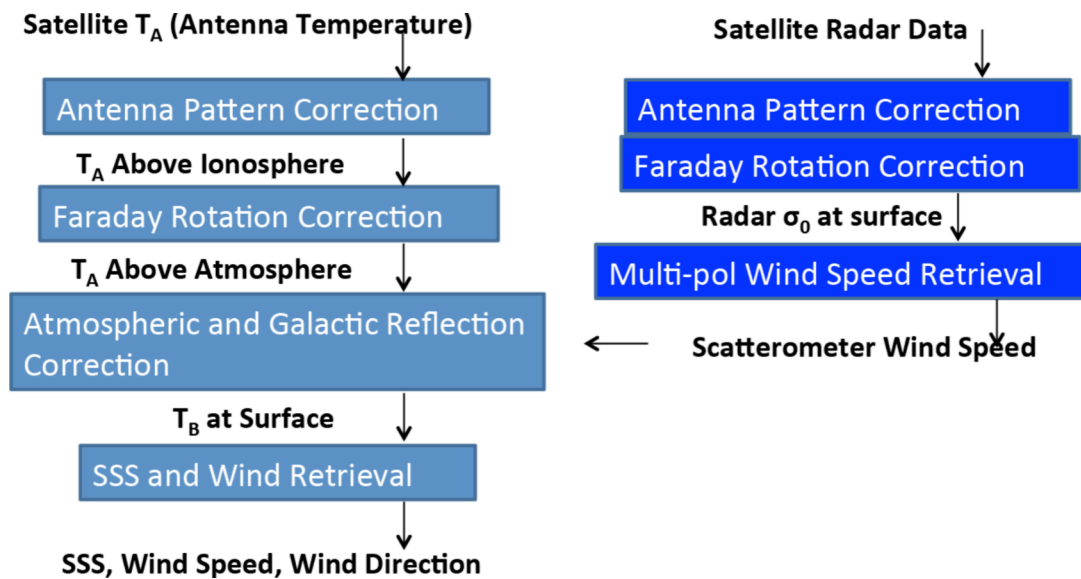


Figure 5. The Aquarius CAP processing block diagram.

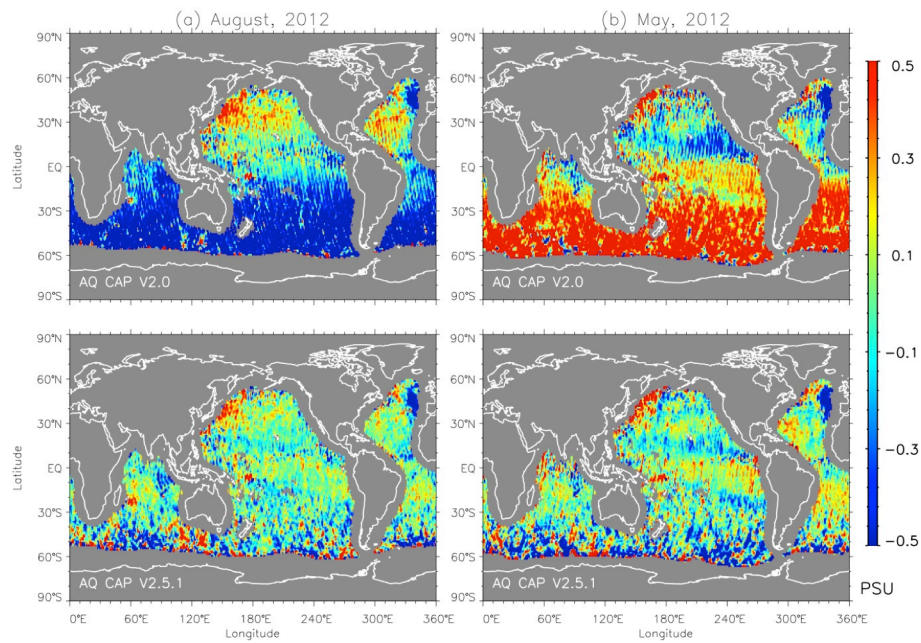


Figure 6. The ascending and descending bias for Aquarius CAP SSS retrievals for two observations periods: (a) August 2012 and (b) May 2012. The upper panels correspond to the CAP v2.0 products corrected using the geometric optics model for the reflection of galactic radiation, while the lower panels for the neural network model (CAP v2.5.1).



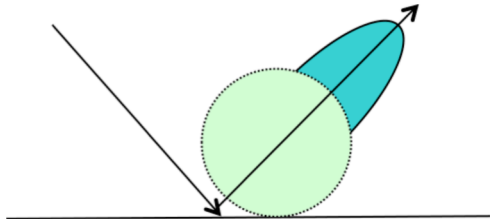


Figure 7. The bistatic scattering of ocean surfaces consists of Geometric optics (blue) and diffused scattering (green) terms. The diffused scattering term nominally has a smaller, but broader scattering pattern than the GO scattering term.

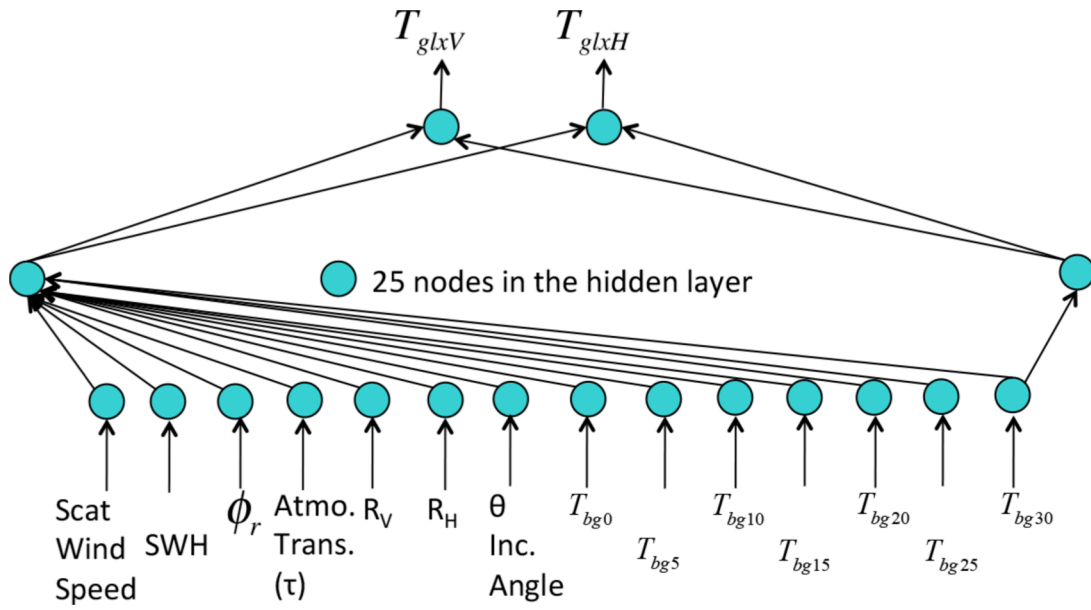


Figure 8. Three-layer perceptron Neural Network used to model the reflected galactic sky radiation for vertical and horizontal polarizations,  $T_{glxV}$  and  $T_{glxH}$ . The network coefficients are trained using the back-propagation algorithm.

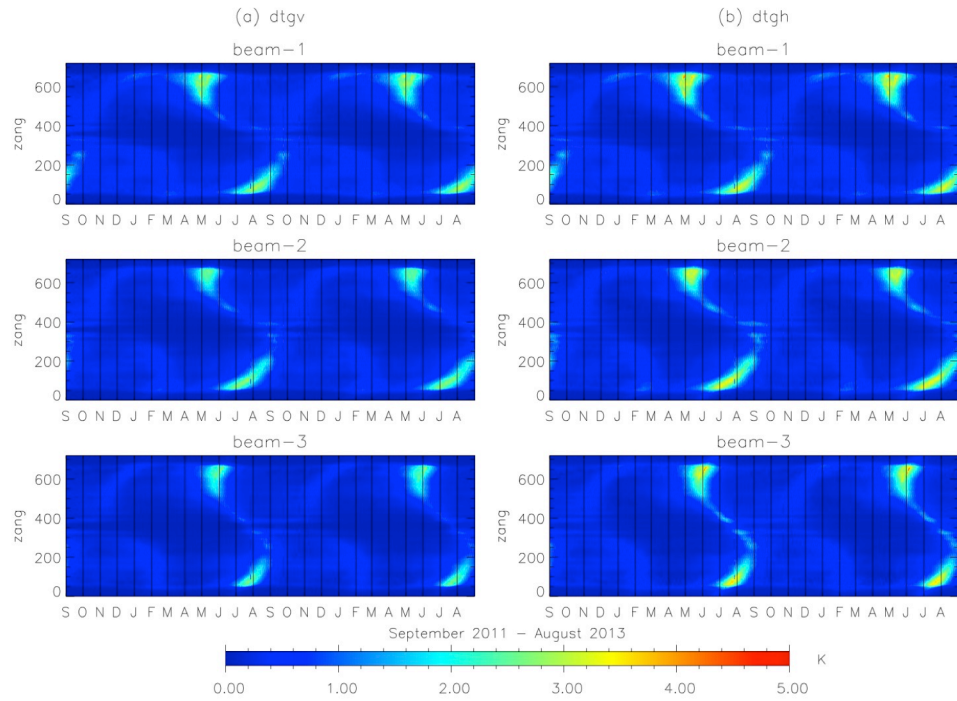


Figure 9. The reflected galactic sky radiation computed using the neural network model versus time and orbit position (zang) of the satellite within an orbit. The value of ‘zang’ corresponds to the angular position of the satellite discretized at 0.5-degree steps for each orbit; its value of 0 to 360 represents the ascending orbit and 360 to 720 the descending. The three panels on the left are for vertical polarization, and three on the right for the horizontal polarization.

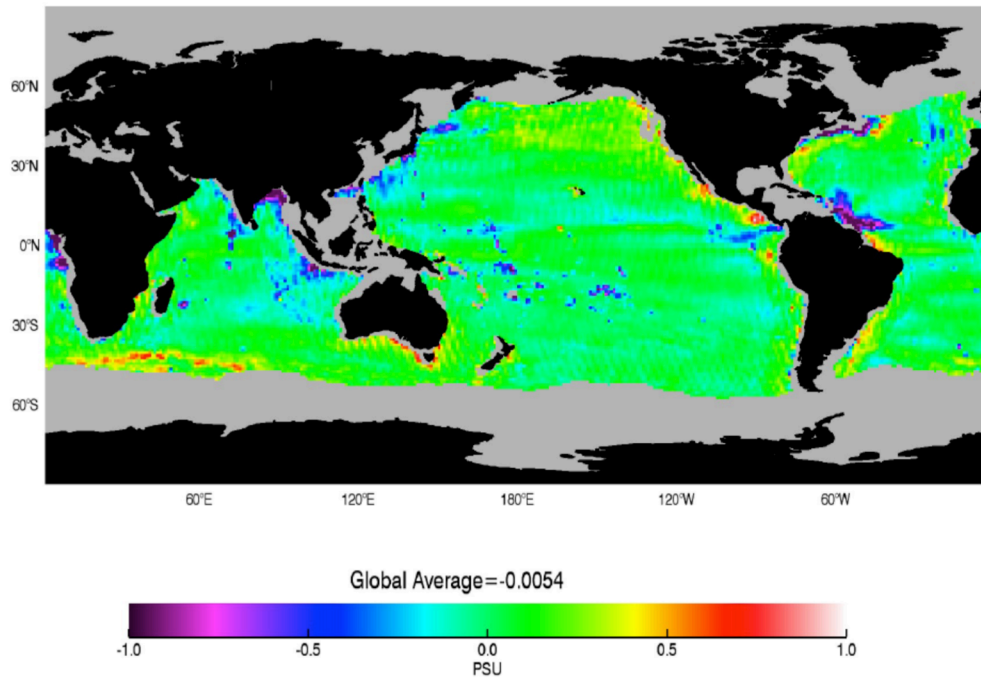


Figure 10. The bias between Aquarius CAP and APDRC SSS for the time period from Sept 2011 to Sept 2013.

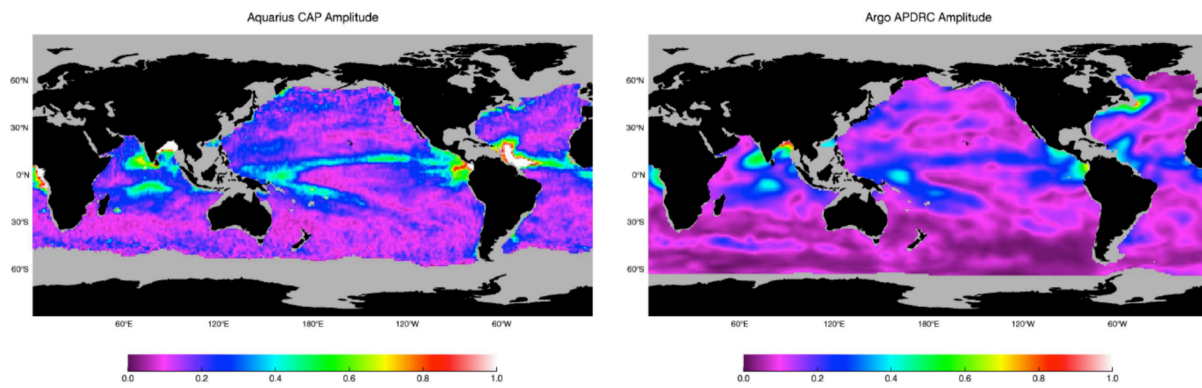


Figure 11. The amplitude of Aquarius CAP and APDRC ARG0 monthly anomalies.

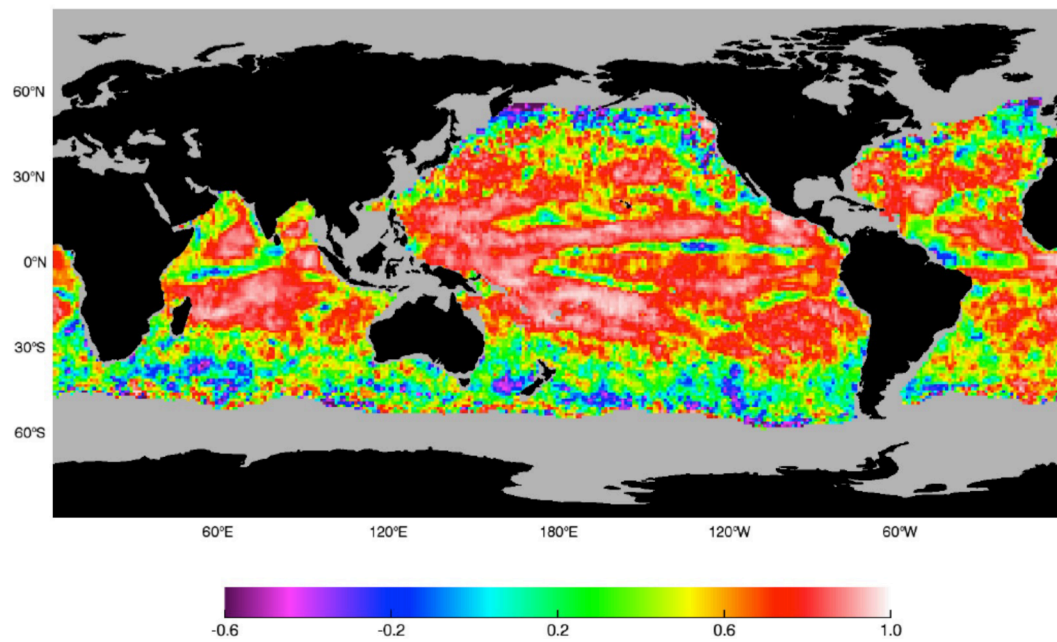


Figure 12. The correlation coefficient between the monthly anomalies of Aquarius CAP and APDRC SSS.

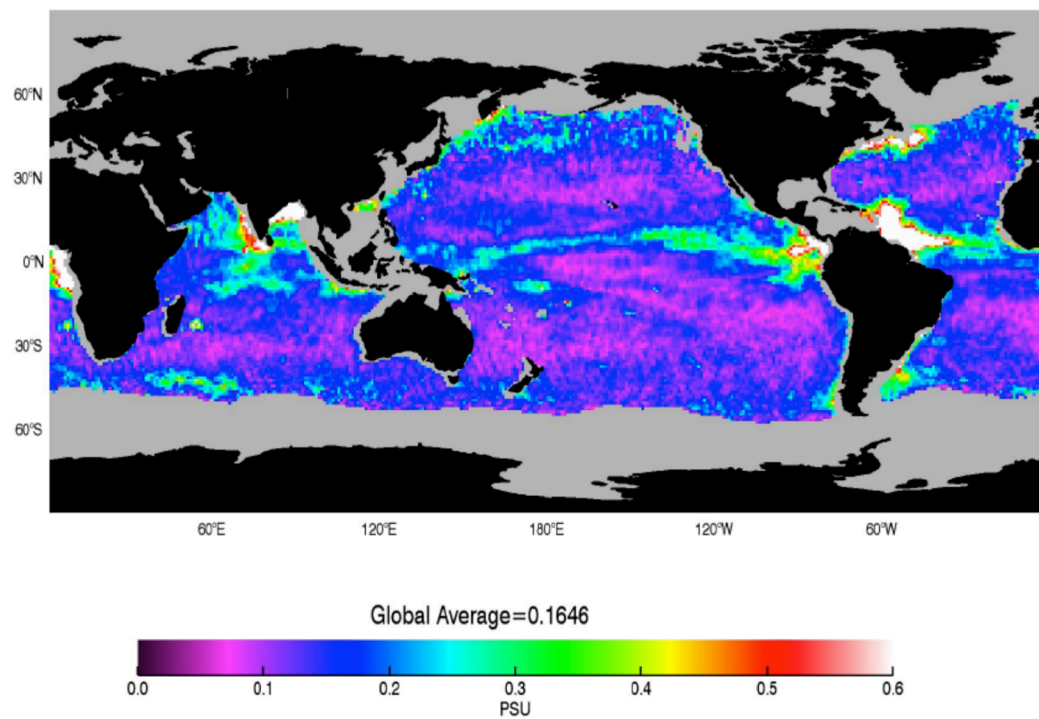


Figure 13. The standard deviation of the differences between Aquarius and APDRC anomalies for the time period from September 2011 to September 2013.

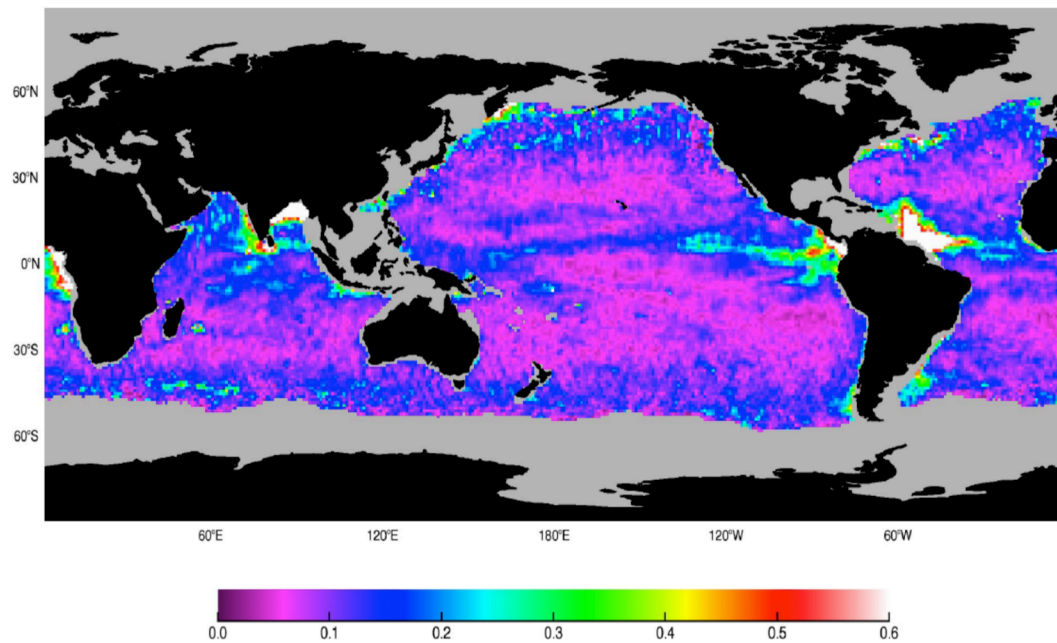


Figure 14. The standard deviation of the uncorrelated differences ( $S_N$ ) between Aquarius and APDRC anomalies for the time period from September 2011 to September 2013.



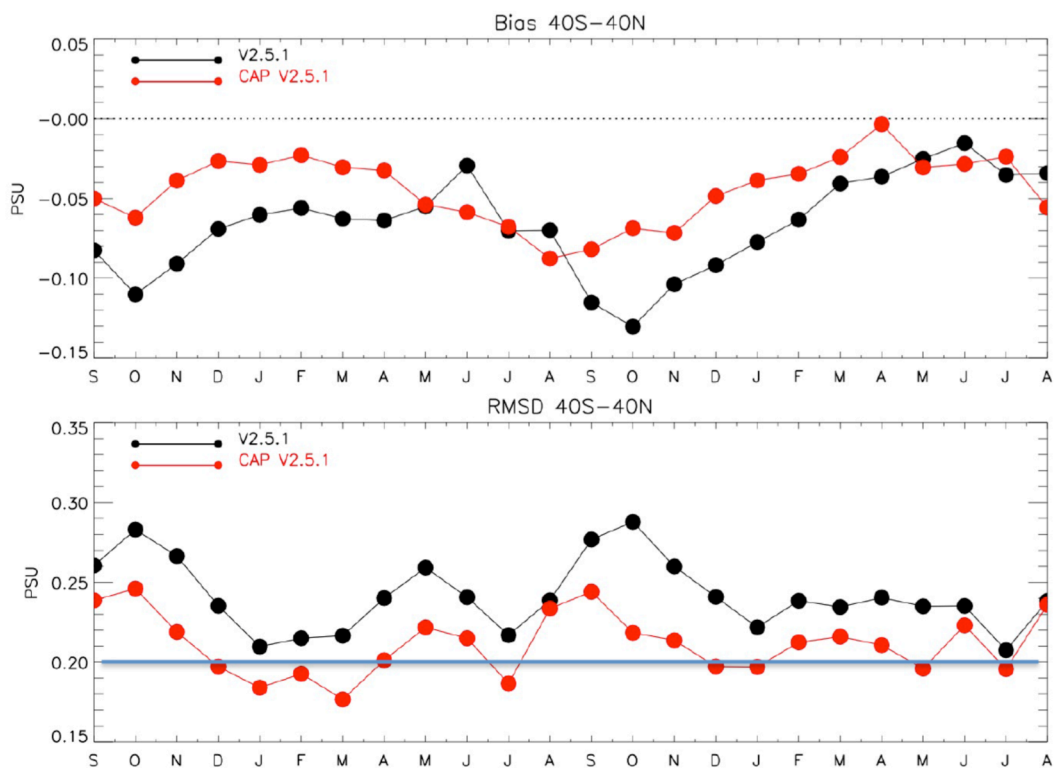


Figure 15. The bias and RMS difference between monthly-averaged Aquarius SSS and APDRC-ARGO monthly gridded product for tropical and mid-latitudes between (40 deg N and 40 deg S). Black dots and curves are for the ADPS-RSS algorithm (v2.5.1). Red dots and curves are for the Aquarius CAP product (CAP v2.5.1).

728

729

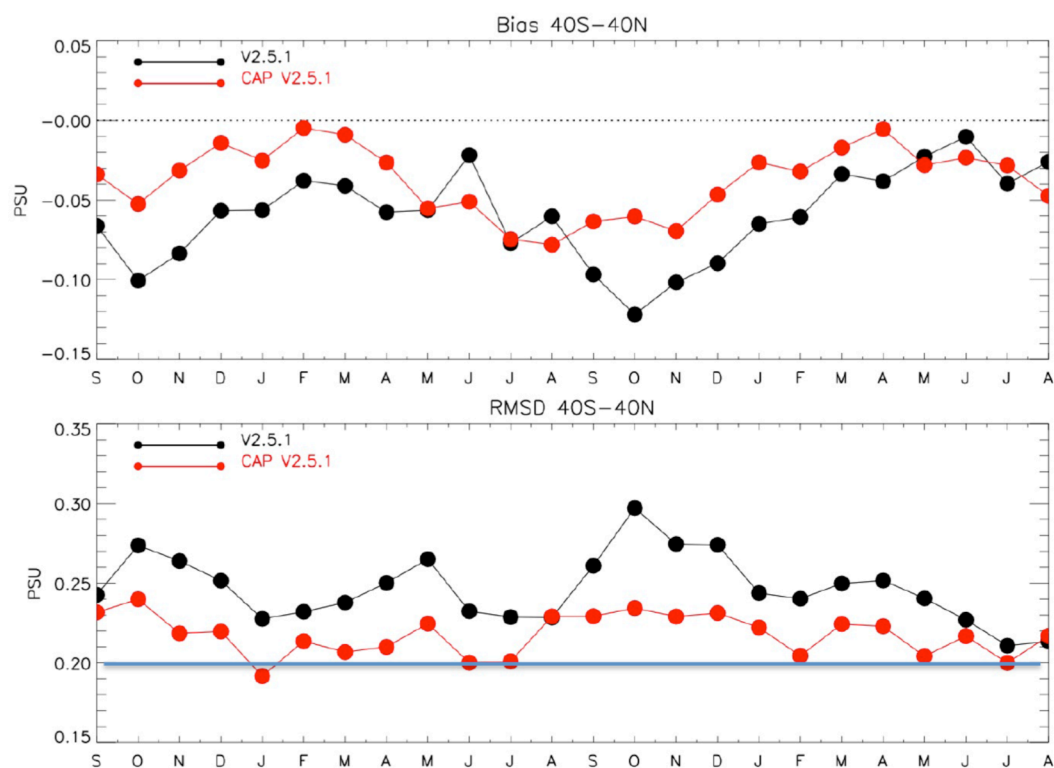


Figure 16. The bias and RMS difference between monthly-averaged Aquarius SSS and JAMSTEC-ARGO monthly gridded product. Black dots and curves are for the ADOPS-RSS algorithm (V2.5.1). Red dots and curves are for the Aquarius CAP product (CAP V2.5.1).